Lithium adsorption on armchair graphene nanoribbons

Dana Krepel, Oded Hod *

School of Chemistry, The Sackler Faculty of Exact Sciences, Tel Aviv University, Tel Aviv 69978, Israel

ARTICLE INFO

ABSTRACT

Lithium adsorption on two dimensional graphene and armchair graphene nanoribbons is studied using advanced density functional theory calculations. The relative stability of different adsorption sites is investigated taking into account different ribbon widths, adsorbate densities, and spin states. We find the singlet spin state to be the true ground state of the systems considered. For this spin state, the binding energy increases with decreasing adatom density due to lower Coulomb repulsion between the partially charged Li atoms. At low adsorbate densities the favorable adsorption sites on the nanoribbons are found to be the hollow sites near the edges of the ribbon, whereas at higher densities, Li atoms tend to couple on next-nearest neighboring hexagons close to the ribbon's edge. Adsorption of the metal atoms is found to significantly decrease the bandgaps of all systems studied, turning them metallic for sufficiently large adatom densities. This suggests lithium doping as a possible route for bandgap engineering of graphitic systems.

© 2010 Elsevier B.V. All rights reserved.

1. Introduction

Since their first successful fabrication [1], graphene nanoribbons (GNRs) have been the focus of extensive experimental and theoretical efforts [2–5]. GNRs, which are elongated stripes cut out of a graphene sheet, have the same unique hexagonal carbon lattice as carbon nanotubes (CNTs), confined to a quasi-one-dimensional structure. Therefore, they share a variety of interesting physical characteristics. Experimental evidence of ballistic electronic transport, large phase coherence lengths, and current density sustainability [5], interesting magnetic properties [6–8], quasi-relativistic behavior [4,9,10], and electronic structure engineering capabilities [11–14] identify low-dimensional graphene as one of the most promising materials for novel nano-electronic and nano-mechanical devices.

Chemical sensing is one of the most promising applications of graphene based nanostructures [15]. The large surface to volume ratio allows for enhanced adsorption of gas molecules [16–19] which, in turn, may alter the electronic properties of the underlying system allowing for efficient detection. Furthermore, the unique electronic structure of graphene, which exhibits vanishing charge carrier densities around the Fermi surface, suggests that even a minute concentration of chemical dopants will cause notable changes in the transport properties of the system allowing for high-sensitivity detection capabilities. This has been recently demonstrated experimentally when room temperature *single molecule* detection capabilities have been achieved using relatively wide GNRs [15]. Nevertheless, one of the main obstacles for the use of graphene

based materials as chemical detectors is the low chemical reactivity of the pristine two-dimensional graphene surface leading merely to physisorption of most chemical species with minor effect on the electronic properties of the substrate. To overcome this problem, chemisorption on lattice defects such as vacancies or edges of the graphene layer has been suggested [20–24]. Alternatively, one may utilize strongly binding alkali-metal atoms as anchoring sites for chemisorptions of otherwise weakly binding molecules [25–27].

The interaction between alkali-metal atoms and graphene-based materials has been the subject of intensive studies, motivated by their catalytic role of gasification reactions [28,29] and hydrogen adsorption [30] in graphitic hosts. Among all alkali-metals, Li has been identified as the most strongly binding atom [31]. While the detailed interaction mechanism is still controversial [32,33], it is commonly accepted that the small atomic radius of lithium, results in shorter intermolecular distances between the $Li^{\delta+}$ atoms and the graphene plane, which cause a stronger cation-metal/π interaction [34]. In a recent study, the adsorption of Li on narrow zigzag graphene nanoribbons (ZGNRs) has been studied extensively [35]. It was shown that binding is strongest near the edges of the ribbon and decreases as one approach its center [35,36]. Furthermore, the electronic properties of the ribbons have been found to be sensitive to the adsorption with evidence of quenching of the magnetic moment in the vicinity of the adsorption site.

In this paper we focus on the adsorption of Li atoms on the surface of armchair graphene nanoribbons (AGNRs). While, as stated above, Li adsorption on AGNRs is believed to be weaker than on ZGNRs [35], the controllable bandgaps of AGNRs [11–14] make them excellent candidates as substrates for chemical detection. Hence, we study in detail the relative stability of different adsorption sites taking into account different ribbon widths, adsorbate densities, and spin states.

* Corresponding author.
  E-mail address: odedhod@tau.ac.il (O. Hod).

Our calculations have been carried out utilizing the Gaussian suite of programs [37]. Spin-polarized calculations have been performed within the local spin density approximation (LSDA) [38,39], the generalized gradient approximation of Perdew et al. (PBE) [40,41], and the screened-exchange hybrid functional developed by Heyd, Scuseria, and Ernzerhof (HSE) [43–46]. Although DFT, even within the generalized hybrid approach, is a ground state theory, the HSE functional has been shown to reproduce experimental optical bandgaps of bulk semi-conductors and to describe the physical properties of graphene-based materials with exceptional success [12,20,47–49]. We use the double-zeta 6-31G** basis set [35,42] noting that the effects of basis set superposition errors (BSSE) [56] in this type of systems have been recently studied in detail and shown to be of minor importance [35]. We have confirmed this finding for the calculation of the binding energies of Li adsorbed on two-dimensional graphene and performed the rest of the calculations neglecting BSSE corrections.

We start by revisiting the problem of Li adsorption on two-dimensional graphene sheets. Previous studies have focused on the adsorption of a single Li atom per unit cell thus limited to the doublet spin state [35,50–53]. In order to examine whether Li adsorption induces spin polarization in these systems, we compare the doublet spin-state results with the singlet and triplet states. First, the doublet states are calculated for three unit cells with increasing sizes representing decreasing dopant densities. We annotate the unit cells by $(N \times M)$ where N stands for the number of zigzag chains and M for the number of carbon dimers along on its zigzag edge [8,13]. Using this notation we choose the (2×4), (2×6) and (4×8) supercells, which consist of 8, 12 and 32 carbon atoms/unit cell, respectively, and a single Li atom (see panels a–c in Fig. 1). The resulting minimum inter-cell Li-Li distances are 0.426 nm for the (2×4) and the (2×6) cells, and 0.852 nm for the (4×8) cell. The singlet and triplet states are then obtained by duplicating the unit cells along the periodic direction, creating (4×4), (4×6) and (8×8) supercells, with 16, 24 and 64 carbon atoms and 2 Li atoms/unit cell (See panel d–f in Fig. 1) [54]. It is well accepted that alkali metal adsorption on graphitic surfaces takes place preferentially on top of the center of a hexagon (hollow site) rather than on top of a C atom or on top of a C–C bond (bridge site) [50–53]. Therefore, we focus on hollow site adsorption (see Fig. 1) verifying that this position is indeed the most stable.

As can be seen in panels a–c in Fig. 2, for all unit cells considered the singlet state is predicted to be the most stable spin state lower by

0.1–0.25 eV/unit cell than the corresponding doublet and triplet states. All three functional approximations considered give consistent qualitative predictions with only minor quantitative differences. Interestingly, the largest singlet/doublet and singlet/triplet differences obtained are for the largest unit cell studied (8×4) indicating the long range nature of the graphene-mediated Li–Li interactions.

As mentioned above, the dominating adsorption mechanism for Li on graphene relies on cation/π interactions due to charge transfer from the Li atom to the graphene π system. Nevertheless, the gain in binding energy due to charge transfer competes with increasing Coulomb repulsion between the partial positive charges on the Li atoms. Therefore, lower dopant densities result in larger charge transfer and stronger binding. This can be clearly seen in Figs. 3 and 4, where calculations of binding energies for both the 2×4 and the 2×6 cells show relatively similar values of less than 1 eV/unit cell and Mulliken charge transfer of ~0.2 electrons from the Li atom to the graphene's π system, whereas these values increase significantly for all functionals for the 4×8 unit cell: binding energy was found to be above 1.2 eV/unit cell and Mulliken charge transfer was of more than 0.5 electrons. These results further exemplify the graphene-mediated Li atoms' repulsive interaction and are in good agreement with previous reports presenting DFT calculations in the 4×8 graphene unit cell containing one adatom per 32 carbon atoms [35,50,52] and the 2×4 graphene unit cell containing one adatom per 8 carbon atoms [52]. We note that our calculations neglect dispersion interactions, therefore, at large separations, under-binding is to be expected [52].

Another interesting finding is the difference in binding energies and Mulliken charge transfer calculated for the different spin states (See lower right panels in Figs. 3 and 4) using the HSE functional for the 2×6 unit cell we find that for the singlet state, the binding energy is 0.91 eV/unit cell at the equilibrium distance (1.83 Å), whereas both the doublet and the triplet spin states give a smaller value of 0.79 eV/unit cell and a larger equilibrium distance of ~1.90 Å. Furthermore, when examining the Mulliken charge transfer, the singlet state shows a slightly higher value of charge transfer of 0.22 electrons whereas both triplet and doublet show a value of ~0.19 electrons. These results demonstrate the difference between the spin states and further suggest the singlet state as the most stable of all three.

Since Li-graphene binding is based on cation/π interactions we now turn to examine the charge transfer at different Li-graphene separations (Fig. 4). Naturally, at very large Li-graphene separations no charge transfer occurs. Upon decrease in the Li-graphene distance
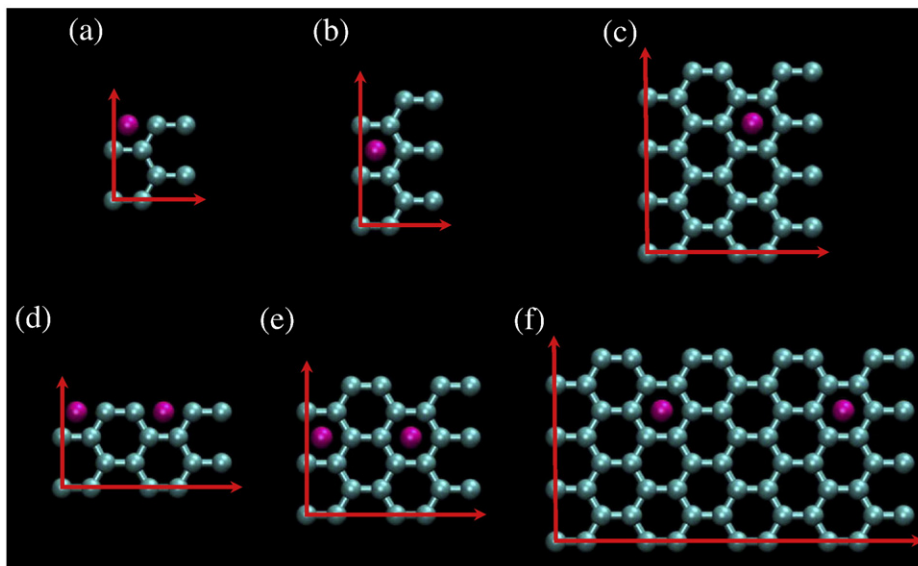
Fig. 1. Schematic diagrams of the (a) 2×4, (b) 2×6 and (c) 4×8 graphene supercells and their (d) 4×4, (e) 4×6 and (f) 8×8 duplications. Representative Li atom locations are marked by magenta circles.
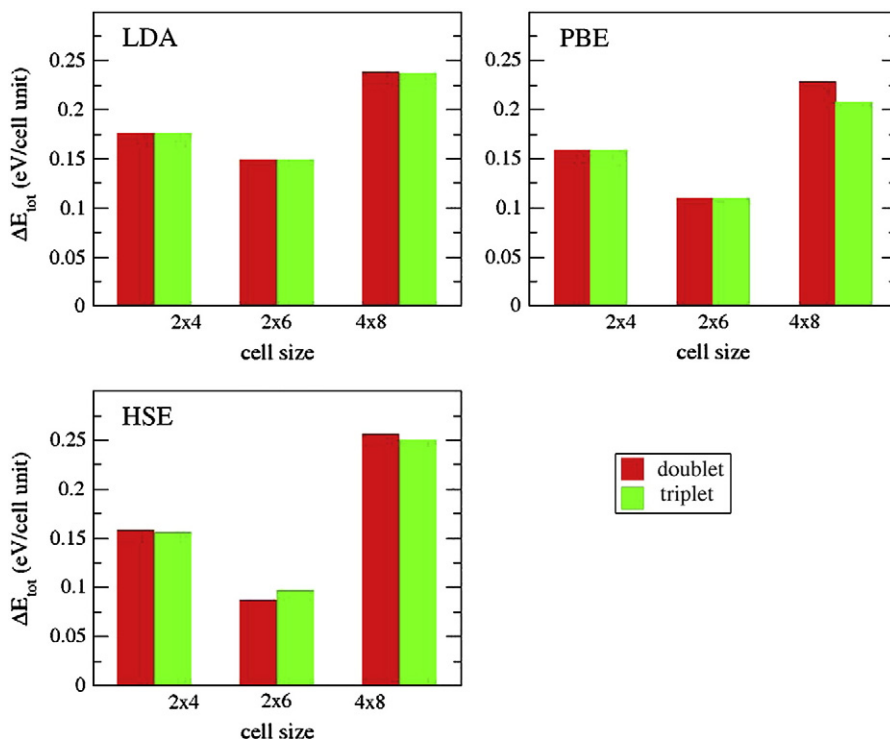
Fig. 2. Total energies of the doublet and triplet spin states with respect to the singlet spin state for the three unit cell sizes studied as calculated using the LDA (upper left panel) PBE (upper right panel) and HSE (lower left panel) functional approximations.

we identify two main regions. At first, one observes an increase in the charge transfer from the Li atoms to the graphene's π-system which, as mentioned above, is countered by electrostatic repulsion between the partially positively charged Li adatoms. At short enough distances (~2 Å depending on the spin state and functional approximation) the charge transfer reaches a maximum value. Further decrease in the Li-

graphene separation results in a decrease in the amount of charge transferred. We associate this decrease in charge transfer with the onset of Pauli repulsions between the electron clouds of the Li atom and the graphene's π-system, as indicated by the steep repulsive behavior at small separations observed in Fig. 3. Interestingly, we find that the distance at which maximum charge transfer is obtained is
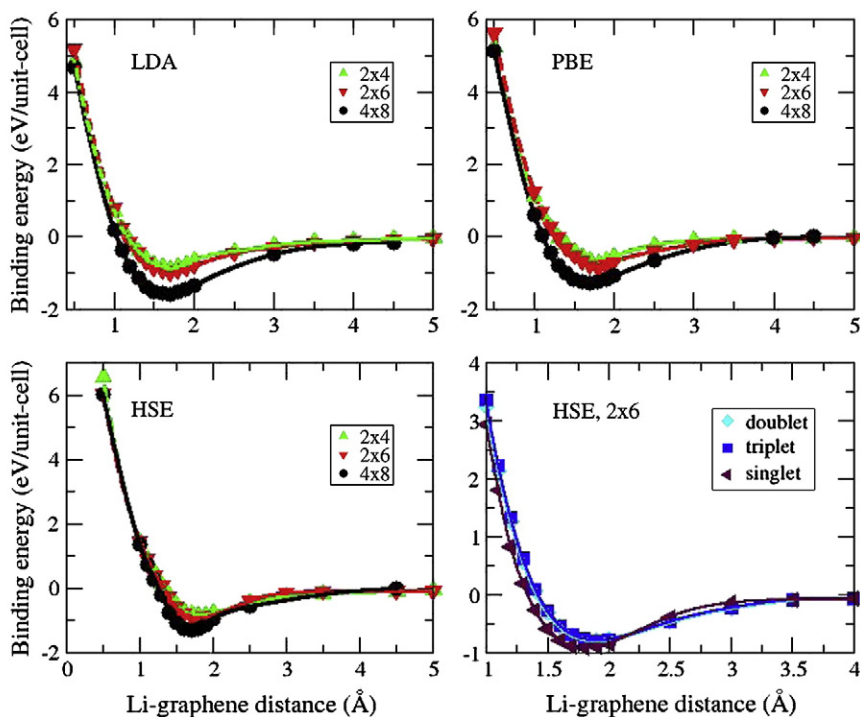
Fig. 3. Binding energy of Li on graphene in the singlet spin state calculated for the (2×4), (2×6) and (4×8) unit cells using the LDA (upper left panel), PBE (upper right panel), and HSE (lower left panel) functionals. Lower right panel: A comparison of the binding energies calculated for the singlet, doublet and triplet spin states using the HSE functional for the 2×6 unit cell.
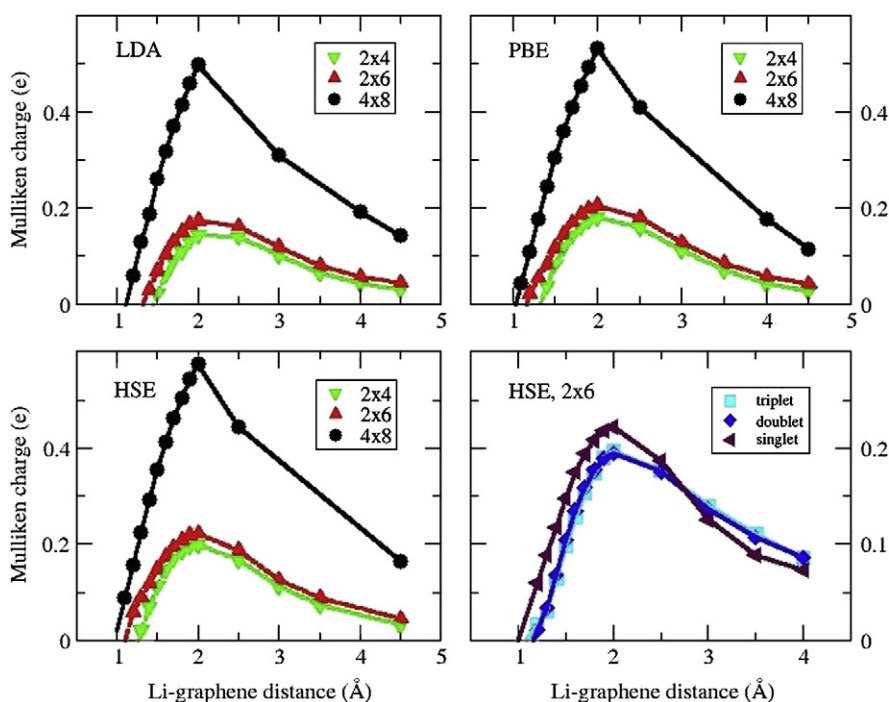
Fig. 4. Mulliken charge transfer between Li and graphene in the singlet spin state calculated for the (2×4), (2×6) and (4×8) unit cells using the LDA (upper left panel), PBE (upper right panel), and HSE (lower left panel) functionals. Lower right panel: A comparison of the Li Mulliken charge for singlet, doublet and triplet spin states using the HSE functional for the 2×6 unit cell.

slightly larger than the Li-graphene equilibrium distance. A possible explanation is that the scaling of the Coulomb repulsion between two adjacent Li atoms, with the partial charge on each such atom, is different than the corresponding scaling of the cation/π interaction, therefore causing the difference in Li-graphene distance at which maximum values are obtained.

In order to better understand this behavior, we examine (see Fig. 5) the charge density and the highest-occupied and lowest-unoccupied crystalline orbitals (HOCO and LUCO) for the 8×8 unit cell, where the charge transfer appears the most significant. Three Li-graphene distances are considered, representing the short distance regime (1.5 Å), the intermediate regime (2.5 Å), and the long range regime
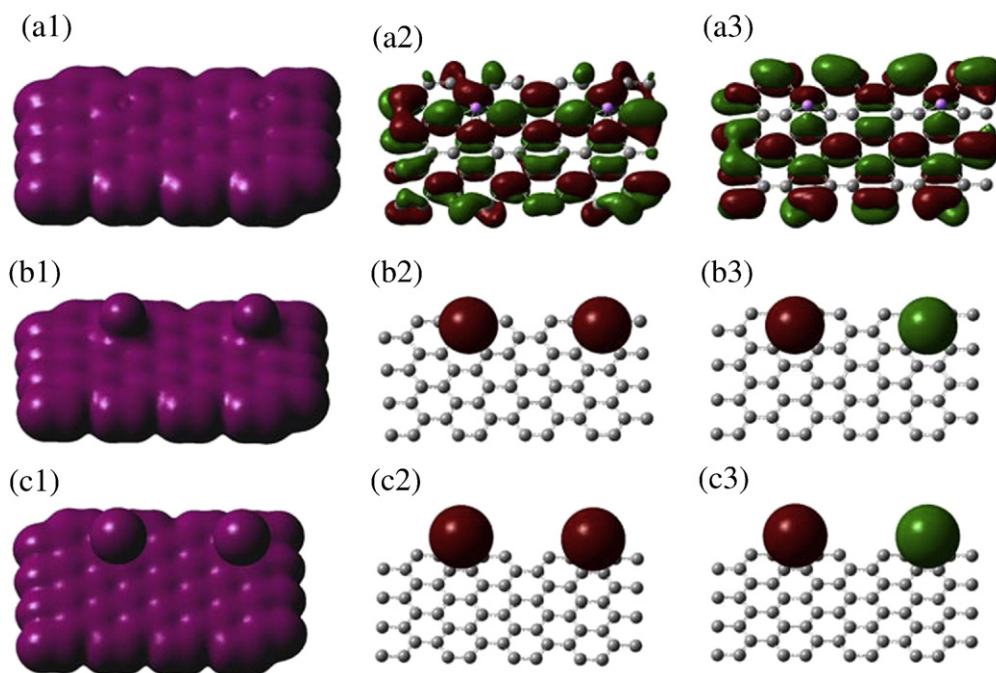
Fig. 5. Charge density (left), HOCO (center) and LUCO (right) crystalline orbitals of the 8×8 unit cell using the HSE functional obtained for representative Li-graphene separations of: 1.5 Å (a1–a3), 2.5 Å (b1–b3) and 4.5 Å (c1–c3). Isosurface values are 0.16 a.u. for the charge density plots and 0.15 a.u. for the orbitals. Similar plots are obtained for the (semi-) local functionals with slight orbital delocalization.

(4.5 Å). In the short distance regime (panels a1–a3 in Fig. 5), there is a small charge density around the Li positions, and the HOCO and LUCO orbitals are concentrated on the graphene surface. As the separation is increased to 2.5 Å (panels b1–b3 in Fig. 5), there is a qualitative change in the nature of the orbitals, which become fully localized on the Li adatoms accompanied with a small overlap between the Li and graphene charge densities. At this point, the cation/π interactions become the dominant factor in the binding of the Li atoms to the graphene surface. At larger separations (panels c1–c3 in Fig. 5) the overlap between the charge densities of the adatoms and the graphene's π-electrons decreases along with the charge transfer, hence the binding is weakened.

Having examined the interactions of Li adatoms with two-dimensional graphene, we now turn to discuss the adsorption of Li atoms on the surface and edges of armchair graphene nanoribbons (ACGNRs). The ribbons considered in the present study are obtained by cutting the two dimensional graphene sheet along its armchair direction while passivating the bare edges with hydrogen atoms, thus creating quasi-one-dimensional structures of finite width. We consider ribbons of three consecutive widths ($N \times 7$), ($N \times 9$), and ($N \times 11$) (0.738 nm, 0.984 nm, and 1.230 nm, respectively) to represent the three subsets of ACGNRs with varying bandgaps [11–14]. For each ribbon width we study two unit cell lengths $N = 2$, 4 (0.426 and 0.852 nm, respectively) giving a total set of 6 different cells, containing 14, 18 and 22 carbon atoms for the shorter cells of increasing width and a density of adsorbed atoms of 2 Li atoms/0.314 nm², 0.419 nm² and 0.524 nm², respectively (see Fig. 6). The adsorption of a single Li atom and 2 atoms/unit cell is considered for each case studied. Within this configuration the Li–Li distance between periodic cells is 0.426 nm for the shorter cells and 0.852 nm for the longer cells. In addition, for the single Li atom per unit cell adsorption scenarios duplications of each cell along the periodic direction were performed to study different spin states [55].

First, we study the relative stabilities of the different Li adsorption sites of ACGNRs. As mentioned above, the hollow sites are the most

stable adsorption positions on ACGNRs and graphene. Therefore, we systematically place a single Li atom on top of all the distinct hollow sites within the unit cells considered (see site numberings in Fig. 6). Fig. 7 compares the total energies of the different adsorption sites at their corresponding equilibrium distances. Similar to the case of ZGNRs [35,36] we find that the most stable Li adsorption sites are at the center of the hexagons close to the edges of the ribbon (position 1 in panels a–f in Fig. 6). We attribute this to the reactive nature of the honeycomb lattice edges. In order to study the effect of different spin states we duplicate the unit cells and compare the results of the doublet spin state obtained with a single atom per unit cell at the edge adsorption site (position 1) to the singlet and triplet states calculated with the duplicated unit cells. For all ACGNRs studied we find that the singlet spin state is the most stable state lower in energy by up to 0.37 eV/Li atom than the corresponding doublet and triplet states (see Fig. 8). Consistent with our findings for two-dimensional graphene as reported above, the largest singlet/doublet and singlet/triplet differences obtained are for the largest unit cell studied (2×11) and (4×11) indicating the long range nature of the graphene-mediated Li–Li interactions in the GNRs systems as well.

Another important aspect of Li adsorption on ACGNRs is its influence on the electronic properties of the ribbon. Fig. 9 presents the bandgaps of the (4×7), (4×9), and (4×11) ACGNRs with (red downward facing triangles) and without (green upward facing triangles) Li adsorption. Focusing on the most favorable adsorption site—the hollow edge site (position 1 in Fig. 6), we consider the singlet spin state and hence use duplicated unit cells with two adsorbed Li atoms per unit cell. The three ribbon widths considered represent the three types of armchair nanoribbons with bandgaps varying from ~0.2 eV to ~2.0 eV. As can be seen, at these adatom densities all systems become metallic regardless of the size of the bandgap associated with the pristine nanoribbon. In order to further explore the effect of adsorption on bandgaps, we study lower adatom densities. Fig. 10 shows the bandgap of the (8×7), (8×9) and (8×11) supercells, with adsorbate densities of 2 Li atoms/1.256 nm²,
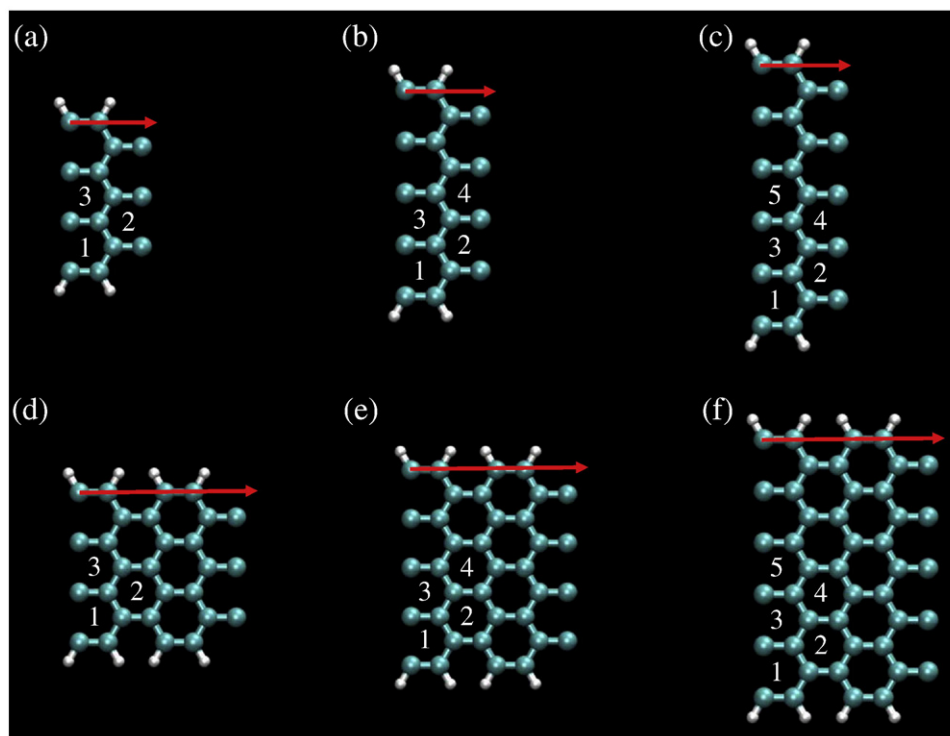
Fig. 6. Schematic diagrams of the GNR supercells used for (a) 2×7, (b) 2×9 and (c) 2×11 calculations and supercells used for (d) 4×7, (e) 4×9 and (f) 4×11 calculations. Numbers represent adsorption hollow sites (above hexagon centers). Red arrows represent the periodic direction.
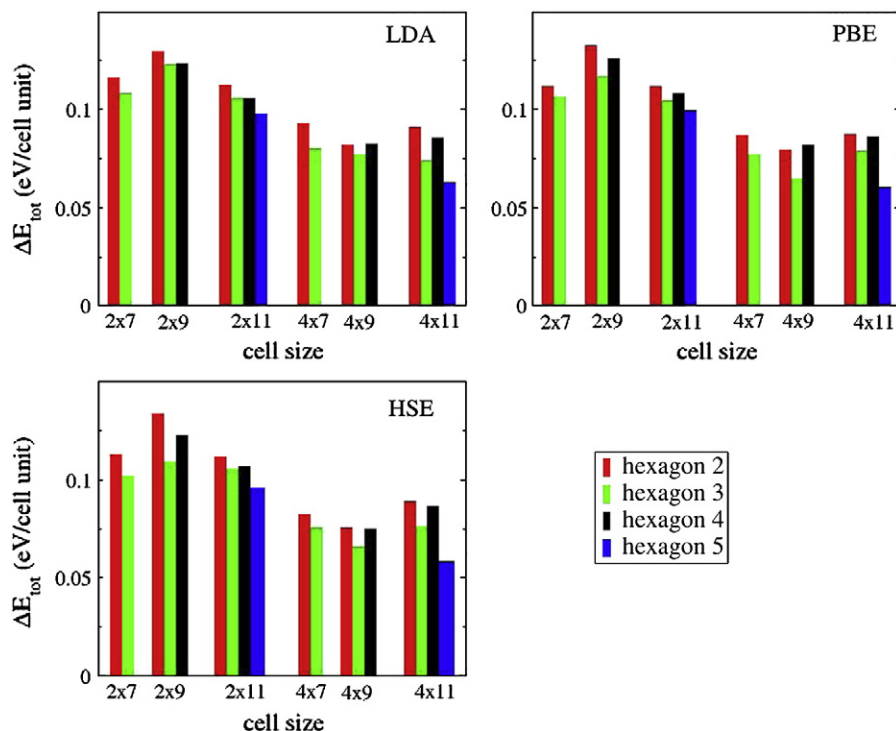
Fig. 7. Singlet total energies as a function of adatom position with respect to the GNR's edge hollow site (position 1), for the six unit cell sizes studied as calculated using the LDA (upper left panel), PBE (upper right panel), and HSE (lower left panel) functional approximations.

1.676 nm^2 and 2.096 nm^2, respectively. Interestingly, only the (8×7) supercell, which is the highest density system, becomes metallic whereas both the (8×9) and the (8×11) systems present small bandgaps, which increase as the adsorbate density decreases. For the adatom densities studied, the highest bandgap was obtained for the 8×11 supercell giving a value of ~0.06 eV using the HSE functional.

Qualitatively, the same results were obtained for both the LDA and the PBE functionals, with bandgap values of 0.009 and 0.008 eV for the 8×9 cell, respectively and 0.024 and 0.013 eV for the 8×11 cell, respectively.

We further analyze the effect of Li adsorption on the electronic properties of the underlying graphene nanoribbon by plotting the
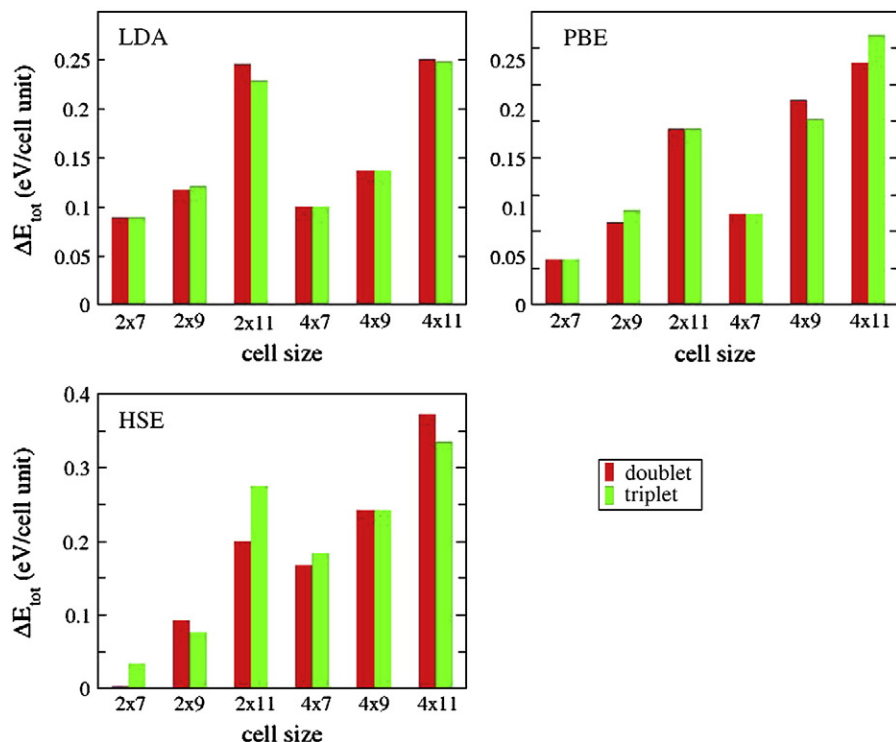
Fig. 8. Total energies of the doublet and triplet spin states with respect to the singlet spin state for the six unit cell sizes studied as calculated using the LDA (upper left panel), PBE (upper right panel), and HSE (lower left panel) functional approximations at the GNR's edge adsorption site (position 1).
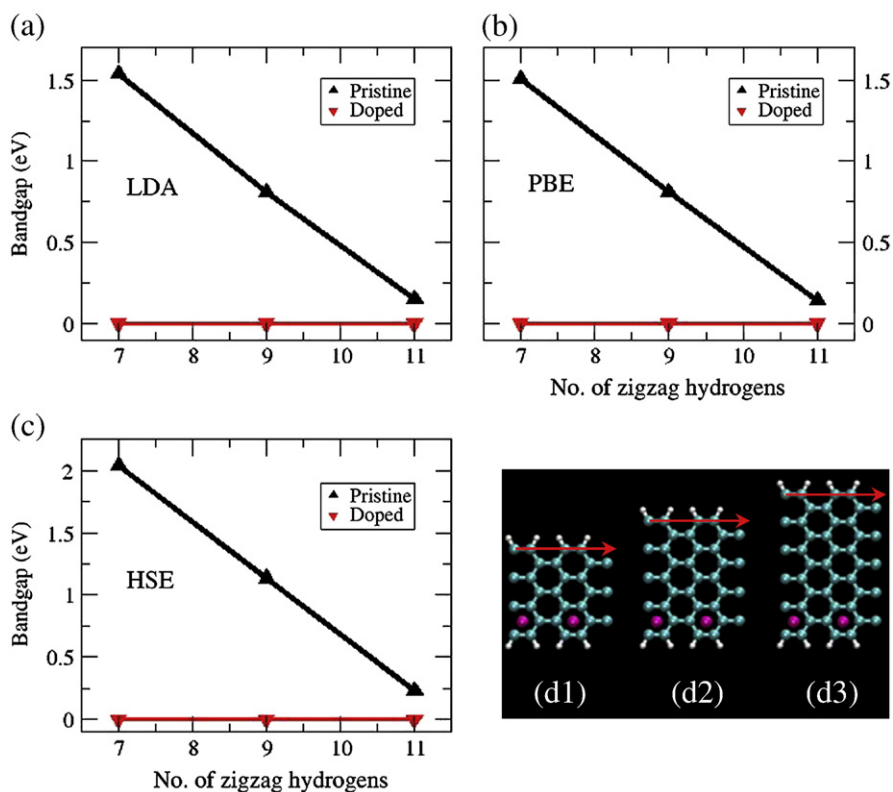
Fig. 9. Dependence of the band gap on the ribbon width for hydrogen-terminated armchair GNRs before (black upward facing triangles) and after (red downward facing triangles) Li adsorption as calculated using the (a) LDA, (b) PBE, and (c) HSE functional approximations. Schematic diagrams of the supercells after duplication used for (d1) 4×7, (d2) 4×9, and (d3) 4×11 calculations. Lithium atoms are marked as magenta spheres, red arrows represent the translational vectors.

total density of states (DOS) in these systems, using the HSE functional. In Fig. 11 we present the total DOS of the pristine GNR (full black line), compared with that of the Li-doped system for the $4 \times M$ unit cells (dashed red line). In each panel the diagrams are aligned such that the original (undoped) midgap point of both systems appears at the origin of the horizontal axis. The Fermi energy of each system is indicated by the colored arrows. As can be seen, Li-doping induces two effects on the electronic structure of the system. The first is a reduction of the orbital energy difference between the original (pristine) HOCO and LUCO. This suggests a mixed Li-graphene nature of these orbitals in the doped-case as is also indicated in Fig. 12. The second effect is a shift in the Fermi energy position due to charge transfer to the graphene surface which clearly induces the metallic nature of the doped systems. Interestingly, despite of orbital mixing,

the size effects observed for the pristine HOCO and LUCO orbital energy differences is preserved in the doped system.

In order to better understand the charge transfer effects on the electronic character of these systems we plotted the charge density and the HOCO and LUCO of the 4×11 and the 8×11 unit cells, focusing on the difference in charge distribution in the larger systems, with smaller adsorbate densities. As can be seen in Fig. 12, the 4×11 unit cell, which was found to be metallic, presents considerable overlap between the charge densities of the Li adatoms (panel a2). Furthermore, the LUCO (panel a4 in Fig. 12) indicates the formation of a Li chain residing on-top of the graphene surface which may serve as a conducting channel turning the system metallic. As the adatom density is decreased (panels b1–b4 in Fig. 12) the formation of a conducting Li chain is prevented due to the increased distance
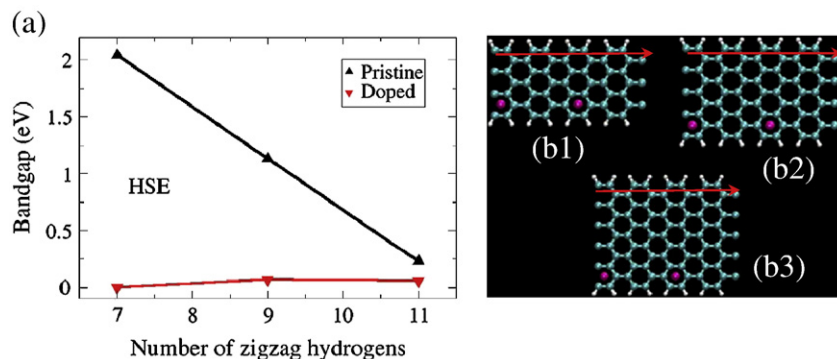
Fig. 10. (a) Dependence of the band gap on the ribbon width for hydrogen-terminated armchair GNRs before (black upward facing triangles) and after (red downward facing triangles) Li adsorption as calculated using HSE functional for lower adsorbent densities. Schematic diagrams of the supercells after duplication used for (b1) 8×7, (b2) 8×9, and (b3) 8×11 calculations at the singlet spin state. Lithium atoms are marked as magenta spheres, red arrows represent the translational vectors.
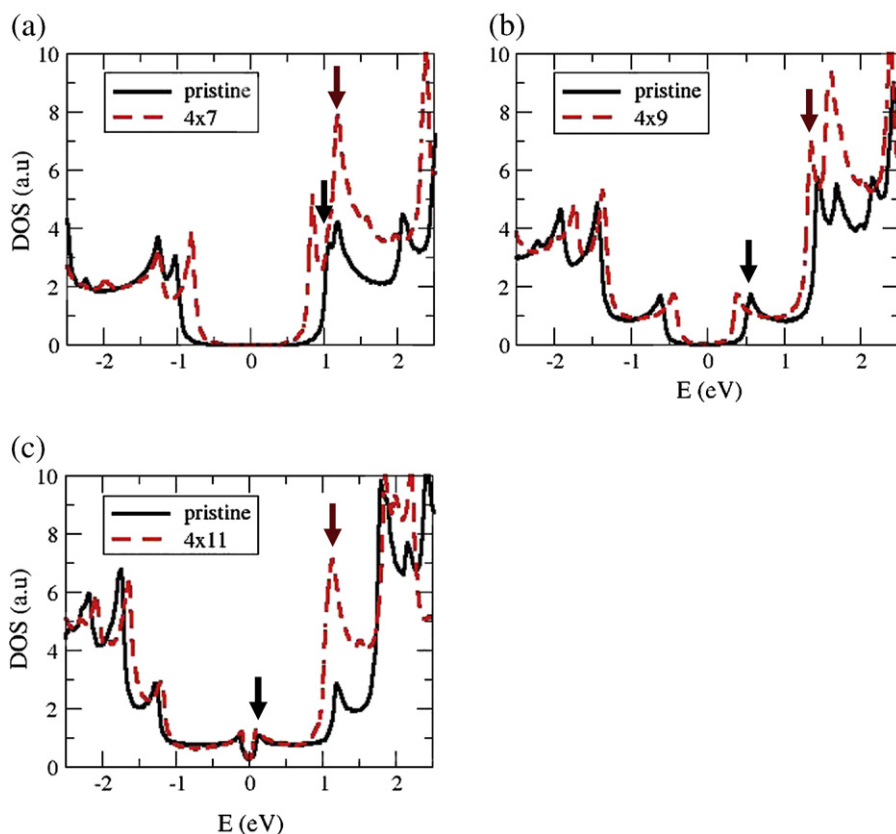
Fig. 11. Comparison of total DOS of pristine (full black line) and Li-doped (red dashed line) $4 \times M$ ribbons (Upper left panel: $M = 7$, upper right panel: $M = 9$, and lower left panel: $M = 11$). All diagrams are aligned such that the original (pristine) midgap point of both systems appears at the origin of the horizontal axis. Fermi energies for each system are indicated by the colored arrows.

between the Li atoms and the decreased charge density around each such atom. While the charge transfer per atom is enhanced, the reduced number of charge donors is not sufficient to turn the system metallic.

Up to now we have considered the adsorption of a single Li atom per nanoribbon unit cell and two adsorbed Li atoms per duplicated unit cells. In order to further study the relative stability of the different Li adsorption sites, we compared the adsorption of 2 Li atoms/unit-cell on all possible couples of hollow sites along the width of the ribbon. As one may expect, for the longer unit cells considered, the

most stable configuration is obtained when the two Li atoms are located above the hollow sites (position 1) of the hexagons close to the opposite edges of the ribbon (see Fig. 13 panels d–f). This is consistent with the recent results calculated for zigzag nanoribbons showing that the edge hollow sites are the most favorable adsorption locations for this system [35,36].

In the case of the shorter unit cells, and therefore larger adsorbate concentrations, the two Li atoms tend to couple such that one Li atom resides on top of a hollow site next to the ribbon's edge (position 1) and the second Li atom adsorbs onto the hollow site of the next-
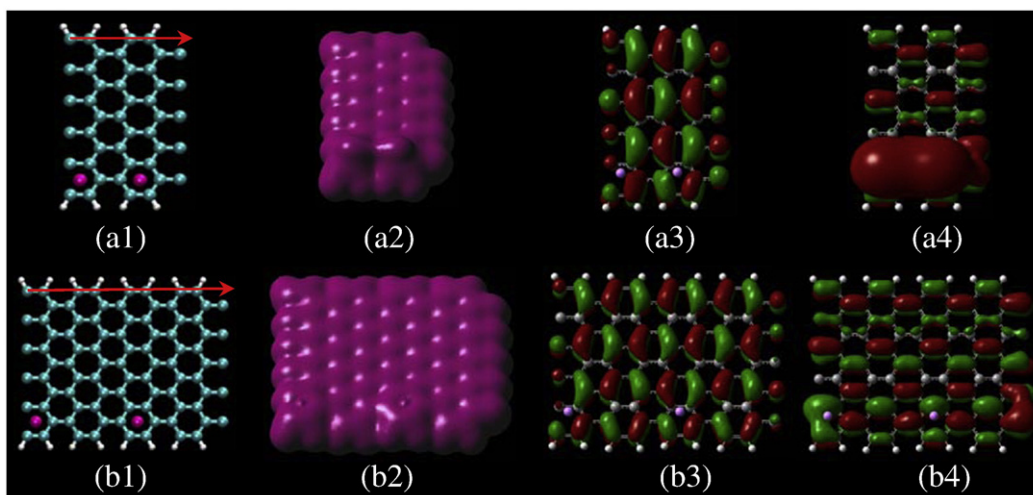
Fig. 12. HSE charge densities (a2 and b2), HOCOs (a3 and b3), and LUCOs (a4 and b4) at the singlet state of the 4×11 (a1) and 8×11 (b1) unit cells systems, respectively. Similar plots are obtained for the (semi-)local functionals with slight orbital delocalization.
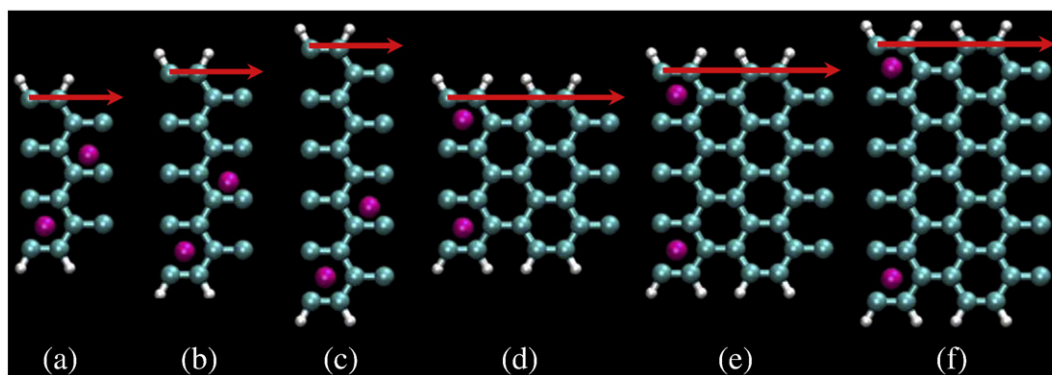
Fig. 13. Schematic diagrams of the GNRs supercells used for the study of the adsorption of two Li adatoms on the surface of the (a) 2×7, (b) 2×9, (c) 2×11, (d) 4×7, (e) 4×9 and (f) 4×11 unit cell systems. Optimal lithium atom positions are marked as magenta spheres, red arrows represent the translational vectors.

nearest-neighbor hexagon (position 4) as shown in Fig. 13 panels a–c. This position is found to be the best compromise between the intra- and inter-cell Coulomb repulsion of the partial positive charges on the Li atoms and the gain in exchange energy due to the coupling between their spins to obtain the singlet ground state. When comparing this configuration to that of two Li adatoms adsorbed on the two edges, the difference in energy increases with the ribbon's width up to 0.18 eV/unit cell for the widest cell considered, demonstrating the significance in coupling the two Li atoms.

Consistent with our previous findings, we find that upon the adsorption of 2 Li atoms/unit cell smaller than 1.048 nm²the other- wise semiconducting ribbons become metallic. Upon duplication of the cells in the periodic direction, now (8×7), (8×9) and (8×11) (once again with adsorbate density of 2 Li atoms/1.256 nm², 1.676 nm² and 2.096 nm² respectively), the largest cell (8×11), with the smallest adsorbate density (2 Li atoms/2.096 nm²) presented small bandgaps of about 0.04 eV, obtained using the HSE fictional, demonstrating once again a threshold of adsorbate density, below which the system remains semi-conducting with a controllable bandgap.

In summary, in this paper we presented a detailed DFT analysis of the adsorption of Li atoms on the surface of both two-dimensional graphene and armchair GNRs. We studied the relative stability of different adsorption sites taking into account different ribbon widths, adsorbate densities, and spin states. Unlike previously reported results for the case of 2D graphene, we found significant singlet/doublet and singlet/triplet total energy differences, suggesting that the singlet spin state is the true ground state of the system. For this spin state, the binding energy was found to increase as the adatoms density decreases due to lower Coulomb repulsion between the partially charged Li atoms which leads to more efficient charge transfer resulting in stronger cation/π interactions. When examining the charge transfer characteristics as a function of Li-graphene distance two regimes have been identified: at infinite separation no charge transfer occurs, as the Li atom approaches the graphene surface charge is transferred from the Li to the graphene π-system thus causing the formation of the cation/π bond. At very short distances (<2 Å) the onset of Pauli repulsions is accompanied with a reduction in charge transfer.

Similar to the case of 2D graphene, the ground state of the Li-GNR system was found to be of singlet nature. Here, at low adsorbate densities the favorable adsorption sites were found to be on top of the hexagons near the edges of the ribbon, whereas at very high densities, one of the Li atoms adsorbs on the edge site while the other adsorbs on the hollow site of the next-nearest-neighbor hexagon. We have also demonstrated the changes in the electronic properties of the GNRs upon the adsorption of Li. Although the adsorption of the metal atom significantly decreased the bandgaps of all cell sizes, the system becomes metallic only for large enough adsorbate densities, showing the formation of conducting Li bridges. With this respect, an interesting research challenge would be to assess the feasibility of this system and exploiting its unique electronic properties as a sensing material for detecting adsorbed molecules at different densities.

References

[1] K.S. Novoselov, A.K. Geim, S.V. Morozov, D. Jiang, Y. Zhang, S.V. Dubonos, I.V. Grigorieva, A.A. Firsov, Science 306 (2004) 666.
[2] A.K. Geim, K.S. Novoselov, Nat. Mater. 6 (3) (2007) 183.
[3] Y. Zhang, Y.W. Tan, H.L. Stormer, P. Kim, Nature 438 (2005) 201.
[4] N.M.R. Peres, A.H. Castro-Neto, F. Guinea, Phys. Rev. B 73 (2006) 195411.
[5] C. Berger, Z. Song, X. Li, X. Wu, N. Brown, C. Naud, D. Mayou, T. Li, J. Hass, A.N. Marchenkov, E.H. Conrad, P.N. First, W.A. de Heer, Science 312 (2006) 1191.
[6] K. Wakabayashi, M. Fujita, H. Ajiki, M. Sigrist, Phys. Rev. B 59 (1999) 8271.
[7] A. Yamashiro, Y. Shimoi, K. Harigaya, K. Wakabayashi, Phys. Rev. B 68 (2003) 193410.
[8] Y.-W. Son, M.L. Cohen, S.G. Louie, Nature 444 (2006) 347.
[9] N.M.R. Peres, A.H. Castro-Neto, F. Guinea, Phys. Rev. B 73 (2006) 241403.
[10] K.S. Novoselov, Z. Jiang, Y. Zhang, S.V. Morozov, H.L. Stormer, U. Zeitler, J.C. Maan, G.S. Boebinger, P. Kim, A.K. Geim, Science 315 (2007) 1379.
[11] M. Ezawa, Phys. Rev. B 73 (2006) 045432.
[12] V. Barone, O. Hod, G.E. Scuseria, Nano Lett. 6 (2006) 2748.
[13] Y.-W. Son, M.L. Cohen, S.G. Louie, Phys. Rev. Lett. 97 (2006) 216803.
[14] M.Y. Han, B. Ozyilmaz, Y. Zhang, P. Kim, Phys. Rev. Lett. 98 (2007) 206805.
[15] F. Schedin, A.K. Geim, S.V. Morozov, E.W. Hill, P. Blake, M.I. Katsnelson, K.S. Novoselov, Nat. Mater. 6 (2007) 652.
[16] J. Zhao, A. Buldum, J. Han, J.P. Lu, Nanotechnology 13 (2002) 195.
[17] S.-H. Jhi, S.G. Louie, M.L. Cohen, Phys. Rev. Lett. 85 (2000) 1710.
[18] Y. Miura, H. Kasai, W. Diño, H. Nakanishi, T. Sugimoto, J. Appl. Phys. 93 (2003) 3395.
[19] A. Allouche, A. Jelea, F. Marinelli, Y. Ferro, Phys. Scr. T124 (2006) 91.
[20] O. Hod, V. Barone, J.E. Peralta, G.E. Scuseria, Nano Lett. 7 (2007) 2295.
[21] N.M.R. Peres, F. Guinea, A.H. Castro-Neto, Phys. Rev. B 73 (2006) 125411.
[22] S.C. Xu, S. Irle, D.G. Musaev, M.C. Lin, J. Phys. Chem. C 111 (2007) 1355.
[23] D. Gunlyke, J. Li, J.W. Mintmire, C.T. White, Appl. Phys. Lett. 91 (2007) 112108.
[24] D.W. Boukhvalov, M.I. Katsnelson, J. Phys.: Condens. Matter 21 (2009) 344205.
[25] H.S. Kang, J. Am. Chem. Soc. 127 (2005) 9839.
[26] Y.H. Zhang, K.G. Zhou, K.F. Xie, J. Zeng, H.L. Zhang, Y. Peng, Nanotechnology 21 (2010) 065201.
[27] A.L. Aguiar, S.B. Fagan, L.B. da Silva, J.M. Filho, A.G.S. Filho, J. Phys. Chem. C 114 (2010) 10790.
[28] K.M. Hock, J.C. Barnard, R.E. Palmer, H. Ishida, Phys. Rev. Lett. 71 (1993) 641.
[29] C. Janiak, R. Hoffmann, P. Sjövall, B. Kasemo, Langmuir 9 (1993) 3427.
[30] I. Cabria, M.J. Lopez, J.A. Alonso, J. Chem. Phys. 123 (2005) 204721.
[31] K. Rytkönen, J. Akola, M. Manninen, Phys. Rev. B 69 (2004) 205404.

[32] J.I. Martínez, I. Cabria, M.J. López, J.A. Alonso, J. Phys. Chem. C 113 (2008) 939.
[33] E. Yoo, J. Kim, E. Hosono, H. Zhou, T. Kudo, I. Honma, Nano Lett. 8 (2008) 2277.
[34] S. Tsuzuki, M. Yoshida, T. Uchimaru, M. Mikami, J. Phys. Chem. A 105 (2001) 769.
[35] C. Uthaisar, V. Barone, J.E. Peralta, J. App. Phys. 106 (2009) 113175.
[36] C. Uthaisar, V. Barone, Nano Lett. 10 (2010) 2838.
[37] M.J. Frisch, G.W. Trucks, H.B. Schlegel, G.E. Scuseria, M.A. Robb, J.R. Cheeseman, J.A. Montgomery Jr., T. Vreven, K.N. Kudin, et al., Gaussian Development Version (Rev. f.1), Gaussian Inc., Pittsburgh, PA, 2008.
[38] J. Slater, Quantum Theory of Molecular and Solids, The Self-Consistent Field for Molecular and Solids, Vol. 4, McGraw-Hill, NewYork, 1974.
[39] S.H. Vosko, L. Wilk, M. Nusair, Can. J. Phys. 58 (1980) 1200.
[40] J.P. Perdew, K. Burke, M. Ernzerhof, Phys. Rev. Lett. 77 (1996) 3865.
[41] J.P. Perdew, K. Burke, M. Ernzerhof, Phys. Rev. Lett. 78 (1997) 1396.
[42] This basis set consists of (3s2p1d) contracted Gaussian functions for C and Li and (2 s 1p) for H.
[43] J. Heyd, G.E. Scuseria, M. Ernzerhof, J. Comp. Phys. 118 (2003) 8207.
[44] J. Heyd, G.E. Scuseria, M. Ernzerhof, J. Comp. Phys. 124 (2006) 219924(E).
[45] J. Heyd, G.E. Scuseria, J. Comp. Phys. 120 (2004) 7274.
[46] J. Heyd, G.E. Scuseria, J. Comp. Phys. 121 (2004) 1187.
[47] O. Hod, J.E. Peralta, G.E. Scuseria, Phys. Rev. B 76 (2007) 233401.
[48] O. Hod, V. Barone, G.E. Scuseria, Phys. Rev. B 77 (2008) 035411.
[49] O. Hod, G.E. Scuseria, ACS Nano 2 (2008) 2243.
[50] F. Valencia, A. Romero, F. Ancilotto, P. Silvestrelli, J. Phys. Chem. B 110 (2006) 14832.
[51] K. Chan, J. Neaton, M. Cohen, Phys. Rev. B 77 (2008) 235430.
[52] M. Khantha, N.A. Cordero, L.M. Molina, J.A. Alonso, L.A. Girifalco, Phys. Rev. B 70 (2004) 125422.
[53] K. Rytkönen, J. Akola, M. Manninen, Phys. Rev. B 75 (2007) 075401.
[54] The reciprocal space integration has been performed in a 180, 120 and 50 uniform k-point grid for the (2×4), (3×4) and the (4×8) graphene cells respectively and 90, 60 30 grids after duplication.
[55] An 80 k-point uniform grid for the one-dimensional nanoribbons of 0.355 nm length and a 40 k-point grid for the 0.781 nm length were chosen (after unit cell duplication 40 and 20 k-point grids were used).
[56] S.F. Boys, F. Bernardi, Mol. Phys. 19 (1970) 553.